PROCEEDINGS OF SPIE

A computationally-efficient bound for the variance of measuring the orientation of single molecules

Wu, Tingting, Ding, Tianben, Mazidi, Hesam, Zhang, Oumeng, Lew, Matthew

SPIE.

Event: SPIE BiOS, 2020, San Francisco, California, United States

A computationally-efficient bound for the variance of measuring the orientation of single molecules

Tingting Wu, Tianben Ding, Hesam Mazidi, Oumeng Zhang, and Matthew D. Lew*

Department of Electrical and Systems Engineering
Washington University in St. Louis, MO 63130, USA

ABSTRACT

Modulating the polarization of excitation light, resolving the polarization of emitted fluorescence, and point spread function (PSF) engineering have been widely leveraged for measuring the orientation of single molecules. Typically, the performance of these techniques is optimized and quantified using the Cramér-Rao bound (CRB), which describes the best possible measurement variance of an unbiased estimator. However, CRB is a local measure and requires exhaustive sampling across the measurement space to fully characterize measurement precision. We develop a global variance upper bound (VUB) for fast quantification and comparison of orientation measurement techniques. Our VUB tightly bounds the diagonal elements of the CRB matrix from above; VUB overestimates the mean CRB by ~34%. However, compared to directly calculating the mean CRB over orientation space, we are able to calculate VUB ~1000 times faster.

Keywords: variance upper bound, Cramér-Rao bound, orientation estimation precision

1. INTRODUCTION

Single-molecule orientation localization microscopy (SMOLM) repeatedly measures both the positions and orientations of sparsely activated single molecules (SMs), such that their images minimally overlap on a camera. Measuring molecular orientation together with position has provided unique insights into the dynamics of DNA conformation under stretching[1] and nanoscale deformations imposed by thermal imprint lithography within polymer films.[2]

Since fluorescent SMs are dipole-like emitters,[3] instruments for measuring SM orientation may leverage 1) a dipole's polarized anisotropic emission pattern[4–6] or 2) the varying excitation probabilities of a dipole under different pumping polarizations.[7] To predict the performance of these techniques, the Cramér-Rao bound (CRB)[8,9] is typically used as it quantifies the limit of measurement variance for any unbiased estimator. However, the CRB is a measurement of local sensitivity at one specific SM orientation, meaning that to understand the global (e.g., average) performance of an orientation measurement technique, one must evaluate the CRB over all possible molecular orientations, which is a computationally expensive process.

In this paper, we develop a global performance metric, termed variance upper bound (VUB). VUB characterizes the diagonal elements of the CRB matrix and tightly bounds it from above. We use VUB to characterize various orientation measurement techniques, and despite VUB being ~1000 times faster to calculate than the average CRB over all of orientation space, the VUB-estimated precision is consistent with those calculated from the average CRB.

2. VARIANCE UPPER BOUND FOR ORIENTATION MEASUREMENT

2.1 Linear Forward Imaging Model

We model a single fluorescent emitter as an oscillating electric dipole with an instantaneous orientational vector $\boldsymbol{\mu} = [\mu_x, \mu_y, \mu_z]$. We also allow the dipole to rotationally diffuse within the integration time of the camera and model this diffusion as an effective rotational constraint γ.[6] A rotationally fixed dipole corresponds to $\gamma = 1$,

---

*mdlew@wustl.edu

while $\gamma = 0$ represents a freely rotating molecule. The intensity distribution of the photons emitted by such a dipole on a camera with n pixels is given by

$$\boldsymbol{I} = s\boldsymbol{B}\boldsymbol{m} + \boldsymbol{b} \in \mathbb{R}^n, \tag{1}$$

where s is the total signal photons collected by the camera, $\boldsymbol{b}$ denotes the background photons in each pixel, $\boldsymbol{m} = \left[\langle \mu_x^2 \rangle, \langle \mu_y^2 \rangle, \langle \mu_z^2 \rangle, \langle \mu_x \mu_y \rangle, \langle \mu_x \mu_z \rangle, \langle \mu_y \mu_z \rangle \right]^T$ is the time-averaged second moment vector of $\boldsymbol{\mu}$, and $\langle \cdot \rangle$ denotes averaging over the imaging acquisition time. The so-called basis matrix $\boldsymbol{B} = [\boldsymbol{B}_{xx}, \boldsymbol{B}_{yy}, \boldsymbol{B}_{zz}, \boldsymbol{B}_{xy}, \boldsymbol{B}_{xz}, \boldsymbol{B}_{yz}] \in \mathbb{R}^{n \times 6}$, which represents the intensity of each camera pixel in response to each component of $\boldsymbol{m}$, may be calculated using vectorial diffraction theory.[4, 10–12] Therefore, the recorded intensity is a linear combination of six basis images weighted by six second moments. Among these parameters, only $\boldsymbol{B}$ is related to the imaging system, while s, $\boldsymbol{m}$, and $\boldsymbol{b}$ are properties of the fluorescent molecules and sample of interest. We seek to develop a metric to characterize the fundamental measurement sensitivity of the imaging system by considering $\boldsymbol{B}$ alone.

2.2 Variance Upper Bound

Fisher information (FI) quantifies the amount of information that a random variable contains regarding some unknown parameter(s). The FI matrix $\boldsymbol{J}$ that quantifies the information that $\boldsymbol{I}$ contains about the orientational second moments $\boldsymbol{m}$ can be written as

$$\boldsymbol{J} = \sum_{i=1}^{n} \frac{1}{I_i} \nabla I_i^T \nabla I_i. \tag{2}$$

The FI matrix is a function of ∇I_i, which is the derivative of the intensity I_i with respect to $\boldsymbol{m}$ at the ith camera pixel, that is,

$$\nabla I_i = \frac{\partial I_i}{\partial \boldsymbol{m}} \tag{3}$$

$$= \left[\partial I_i / \partial \langle \mu_x^2 \rangle \quad \partial I_i / \partial \langle \mu_y^2 \rangle \quad \partial I_i / \partial \langle \mu_z^2 \rangle \quad \partial I_i / \partial \langle \mu_x \mu_y \rangle \quad \partial I_i / \partial \langle \mu_x \mu_z \rangle \quad \partial I_i / \partial \langle \mu_y \mu_z \rangle \right] \tag{4}$$

$$= s\boldsymbol{B}_i, \tag{5}$$

where $\boldsymbol{B}_i \in \mathbb{R}^{1 \times 6}$ donates the ith row of $\boldsymbol{B}$. Rewriting $\boldsymbol{J}$, we have

$$\boldsymbol{J} = \sum_{i=1}^{n} \frac{s^2}{I_i} \boldsymbol{B}_i^T \boldsymbol{B}_i \triangleq \hat{\boldsymbol{A}}^T \boldsymbol{C}^T \boldsymbol{C} \hat{\boldsymbol{A}}. \tag{6}$$

Here, we introduce $\hat{\boldsymbol{A}} \in \mathbb{R}^{n \times 6}$, whose entries are given by

$$\hat{A}_{ij} = \frac{sB_{ij}}{\sqrt{s \|\boldsymbol{B}_i\| + b_i}}, \tag{7}$$

and $\boldsymbol{C} \in \mathbb{R}^{n \times n}$, which can be written as

$$\boldsymbol{C} = \begin{bmatrix} \frac{\sqrt{s\|\boldsymbol{B}_1\| + b_1}}{\sqrt{s\boldsymbol{B}_1 \boldsymbol{m} + b_1}} & 0 & \cdots & 0 \\ 0 & \frac{\sqrt{s\|\boldsymbol{B}_2\| + b_2}}{\sqrt{s\boldsymbol{B}_2 \boldsymbol{m} + b_2}} & \cdots & 0 \\ \vdots & \vdots & \ddots & \vdots \\ 0 & 0 & \cdots & \frac{\sqrt{s\|\boldsymbol{B}_n\| + b_n}}{\sqrt{s\boldsymbol{B}_n \boldsymbol{m} + b_n}} \end{bmatrix}. \tag{8}$$

The Cauchy-Schwarz inequality implies $\boldsymbol{B}_i \boldsymbol{m} \leq \|\boldsymbol{B}_i\| \|\boldsymbol{m}\|$. Since $\|\boldsymbol{\mu}\| = 1$ for any SM transition dipole, $\|\boldsymbol{m}\| \leq 1$ for all possible dipole orientations. Therefore, all diagonal elements C_{jj} are larger than 1. We therefore define our VUB matrix $\boldsymbol{\Gamma}$ from Equation (6) as

$$\boldsymbol{\Gamma} \triangleq (\hat{\boldsymbol{A}}^T \hat{\boldsymbol{A}})^{-1}. \tag{9}$$

Given a CRB matrix $\boldsymbol{R} = \boldsymbol{J}^{-1}$, the ith eigenvalue β_i of $\boldsymbol{R}$ is equal to the inverse of ith eigenvalue λ_i^{-1} of $\boldsymbol{J}$. Since $\boldsymbol{J}$ and $\boldsymbol{\Gamma}$ are positive semidefinite matrices, the ith eigenvalue γ_i of $\boldsymbol{\Gamma}$ satisfies

$$\gamma_i \geq \lambda_i^{-1} = \beta_i. \tag{10}$$

We therefore have

$$\Gamma_{jj} \geq R_{jj} = [\boldsymbol{J}^{-1}]_{jj}. \tag{11}$$

In other words, the jth diagonal element Γ_{jj} of $\boldsymbol{\Gamma}$ bounds the CRB variance R_{jj} of m_j from above.

2.3 Variance Upper Bound for Subset of Orientatioanl Moments

We next modify VUB to evaluate a subset of orientational second moments. Here, we assume the average orientation of a SM lies within a plane perpendicular to the optical axis (hereafter referred to as in-plane), i.e., $\langle \mu_z \rangle = 0$. In this case, only the 2D second moments $\boldsymbol{m}_{2\text{D}} = [\langle \mu_x^2 \rangle, \langle \mu_y^2 \rangle, \langle \mu_z^2 \rangle, \langle \mu_x \mu_y \rangle]$ and the 2D basis matrix $\boldsymbol{B}_{2\text{D}} = [\boldsymbol{B}_{xx}, \boldsymbol{B}_{yy}, \boldsymbol{B}_{zz}, \boldsymbol{B}_{xy}]$ are of interest for characterizing estimation precision. We now have a 2D CRB matrix $\boldsymbol{R}_{2\text{D}}$ expressed as

$$\boldsymbol{R}_{2\text{D}} = \boldsymbol{J}_{2\text{D}}^{-1} = \left(\sum_{i=1}^{n} \frac{s^2}{I_i} \boldsymbol{B}_{2D,i}^T \boldsymbol{B}_{2D,i} \right)^{-1}. \tag{12}$$

Similar to the 3D case, we now define an in-plane VUB matrix $\boldsymbol{\Gamma}_{2\text{D}}$ as

$$\boldsymbol{\Gamma}_{2\text{D}} = \left(\hat{\boldsymbol{A}}_{2\text{D}}^T \hat{\boldsymbol{A}_{2\text{D}}} \right)^{-1}, \tag{13}$$

where each entry of $\hat{\boldsymbol{A}}_{2\text{D}}$ is given by

$$\boldsymbol{A}_{2\text{D},ij} = \frac{s B_{2\text{D},ij}}{\sqrt{s \|\boldsymbol{B}_{2\text{D},i}\| + b_i}}. \tag{14}$$

The VUB matrix corresponding to other subsets of the second moments can be derived similarly.

3. VUB CHARACTERIZATION

3.1 Emission Dipole Orientation Measurements using Engineered PSFs

One class of techniques probes the orientation of an SM's emission dipole. To perform an orientation measurement, this orientation must be encoded into the image produced by the microscope. Since a dipole's emission pattern is anisotropic, an orientation-dependent point spread function (PSF) can be generated by placing a well-designed phase mask at the back focal plane of an imaging system. Here, we explore four methods: 1) the polarized (standard) PSF, 2) a defocused PSF[4] (i.e., defocusing the microscope objective by 1 μm out of the water and capturing x- and y-polarized fluorescence on two separate areas of a camera), 3) the bisected PSF,[5] and 4) the tri-spot PSF.[6] Basis images $\boldsymbol{B}$ of these PSFs are shown in Figure 1.

We calculate the bound of the total variance of measuring all six second moments, given by the sum of the diagonal elements Γ_Σ of the VUB matrix. We compare this bound Γ_Σ to the sum of the diagonal elements R_Σ of the CRB matrix for fixed dipoles ($\gamma = 1$) of various orientations (μ_x, μ_y) (Figure 2). For these simulated measurements, we use 380 signal photons and 2 background photons per pixel. The summed VUBs of each PSF ($\Gamma_{\Sigma,\text{polarized}} = 0.7577$, $\Gamma_{\Sigma,\text{defocused}} = 0.4674$, $\Gamma_{\Sigma,\text{bisected}} = 0.5900$, $\Gamma_{\Sigma,\text{tri-spot}} = 0.2501$) are consistent with the sums of the CRBs averaged over all molecular orientations for each PSF ($R_{\Sigma,\text{polarized}} = 0.4731$, $R_{\Sigma,\text{defocused}} = 0.4315$, $R_{\Sigma,\text{bisected}} = 0.4558$, $R_{\Sigma,\text{tri-spot}} = 0.1977$). Overall, VUB overestimates the summed CRB by 34% across the four PSFs, but calculating the VUB is ~1000 times faster than averaging the summed CRB over 2500 sampling points in orientation space. We observe that the error varies dramatically for the polarized standard PSF (Figure 2(a)) across orientation space; these errors likely stem from the elements of $\boldsymbol{C}$ being significantly larger than one, a consequence of the weak intensity contrasts in the $\boldsymbol{B}_{xz}$ and $\boldsymbol{B}_{yz}$ basis images (Figure 1(a)).

We next explore how the VUB Γ_Σ changes for various signal-to-background ratios (SBRs), both for emitters rotating in 3D space (Figure 3(a)) and within the xy plane (Figure 3(b)). We also calculate the peak SBR SBR_{max} across all camera pixels to show the relative detectabilities of each PSF. While the tri-spot PSF shows
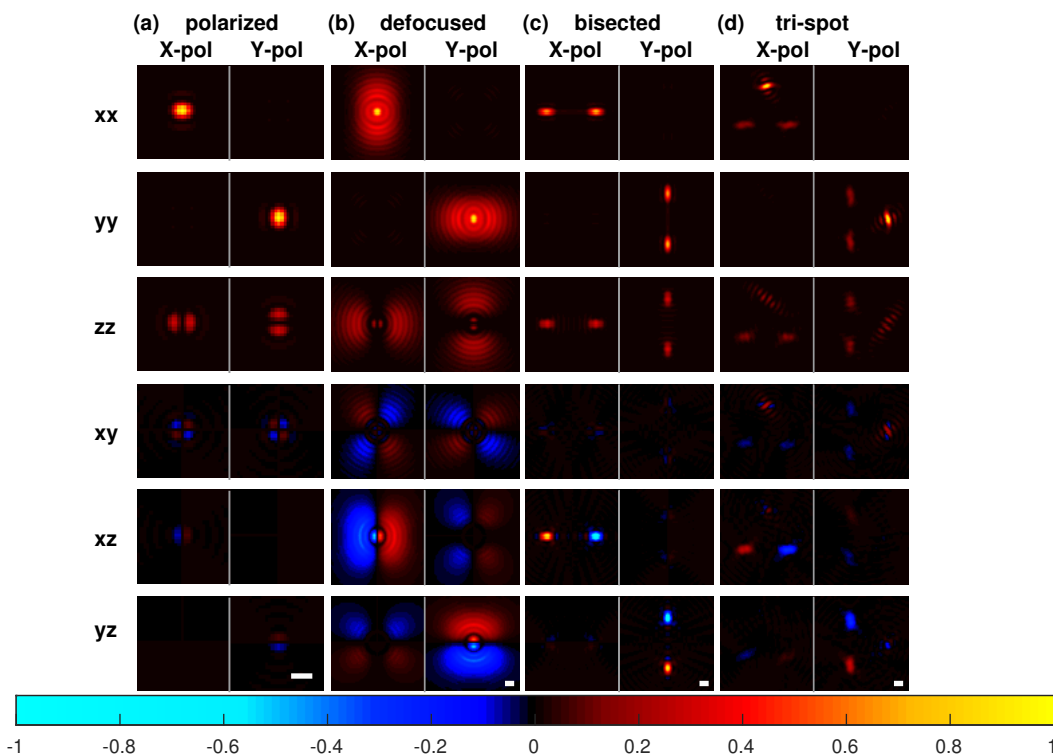
Figure 1. Normalized orthogonally polarized (X-pol and Y-pol) basis images of the (a) standard, (b) defocused (1 μm out of water), (c) bisected, and (d) tri-spot PSFs for emitters at a glass-water interface. Images are normalized in each column. Scale bars: 400 nm.

the best estimation precision for 3D orientation measurements, its $\text{SBR}_{\max}$ is small since photons are separated into three spots across two polarization channels (Figure 1(d)). The tri-spot PSF therefore is more suitable for orientation measurements at high SBRs. The polarized PSF has the highest detectability (i.e., $\text{SBR}_{\max}$) and shows superior estimation precision for in-plane oriented molecules. This observation is confirmed by the high intensity contrasts among the first four basis images (Figure 1(a)).

3.2 Excitation Dipole Orientation Measurement with Pumping Modulation

The probability of an SM to be excited by a photon is proportional to $|\boldsymbol{E} \cdot \boldsymbol{\mu}|^2$, where $\boldsymbol{E}$ represents the electric field of the pumping light. Therefore, by exciting the dipole with varying electric field polarizations, the measured fluorescence intensity can be used to measure its orientation $\boldsymbol{m}$. Here, we analyze the performance of modulating
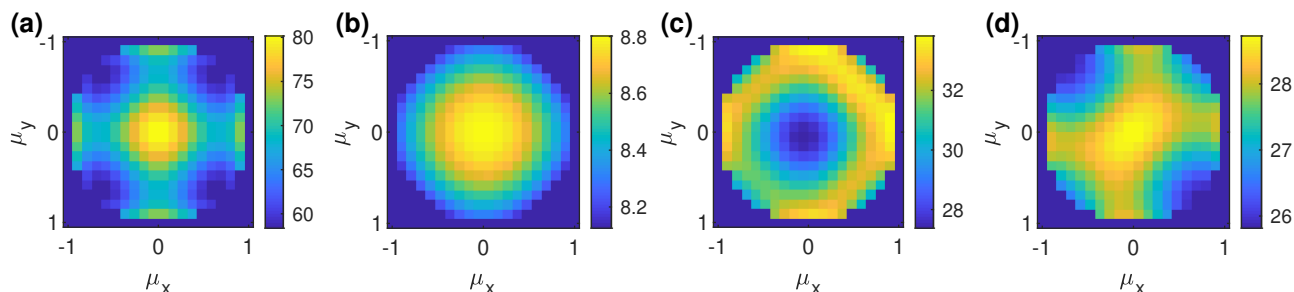

Figure 2. Percent error of the sum Γ_Σ of the diagonal elements of the variance upper bound (VUB) matrix $\boldsymbol{\Gamma}$ relative to the sum R_Σ of the diagonal elements of the CRB matrix $\boldsymbol{R}$ across six second moments for the (a) polarized (67% average error), (b) defocused (7% average error), (c) bisected (31% average error), and (d) tri-spot PSFs (28% average error). These variance bounds are calculated for fixed emitters ($\gamma = 1$) of various orientations (μ_x, μ_y) located at the water-glass interface. We simulated these variances for 380 signal photons detected and 2 background photons detected per pixel.
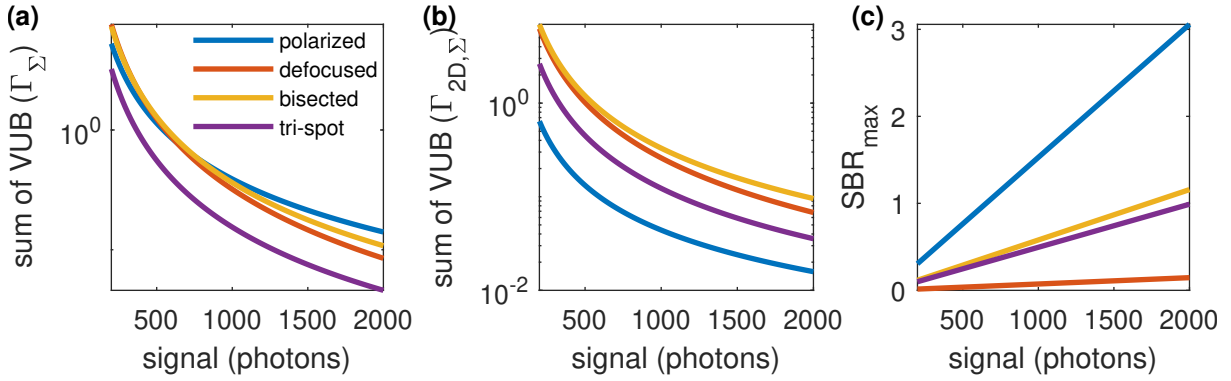
Figure 3. Orientation measurement performance as a function of signal photons. (a) Sum Γ_Σ of VUB $\mathbf{\Gamma}$ over six second moments for molecular orientations in 3D. (b) Sum $\Gamma_{2D,\Sigma}$ of VUB $\mathbf{\Gamma}_{2D}$ (Equation (13)) over the first four second moments for emitters oriented in-plane. (c) Peak SBR ($\text{SBR}_{\max}$) across all camera pixels for rotationally free molecules ($\gamma = 0$). Blue: polarized, red: defocused, yellow: bisected, purple: tri-spot PSF. For all simulations, a background of 10 photons per pixel was used.

pumping polarization for measuring a dipole's in-plane angle (ϕ and in-plane γ).[7] We simulate the case of three sequential fluorescence measurements, i.e., three in-plane linear pumping polarizations $\mathbf{E} = [\mathbf{E_1}, \mathbf{E_2}, \mathbf{E_3}]$, whose polarization axes are 60° apart. A simple basis matrix $\mathbf{B}$ for this measurement is given by

$$\mathbf{B} = [\mathbf{B}_{xx}, \mathbf{B}_{yy}, \mathbf{B}_{xy}] = \begin{bmatrix} E_{1,x}^2 & E_{1,y}^2 & 2E_{1,x}E_{1,y} \\ E_{2,x}^2 & E_{2,y}^2 & 2E_{2,x}E_{2,y} \\ E_{3,x}^2 & E_{3,y}^2 & 2E_{3,x}E_{3,y} \end{bmatrix},$$
(15)

where $E_{i,x/y}$ represents x/y polarization component of the ith pumping polarizations. We calculate the VUB Γ_{jj}
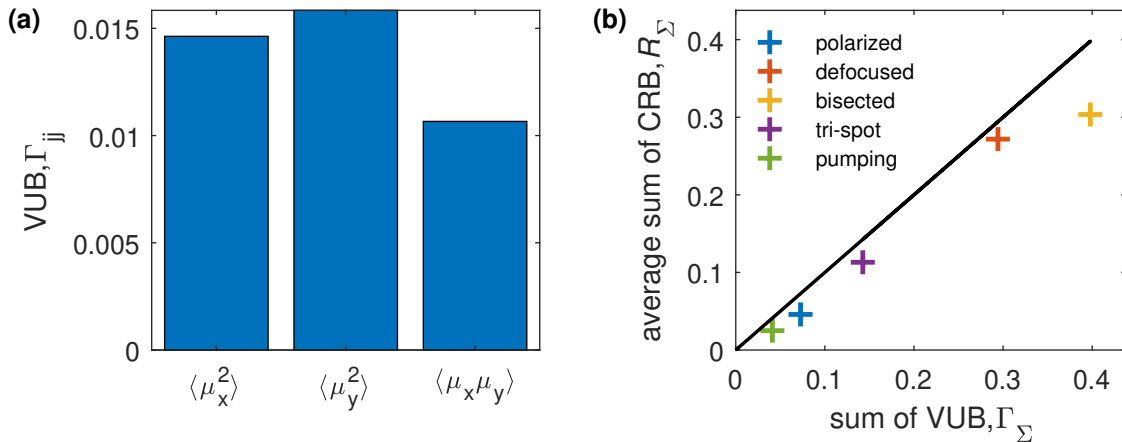

Figure 4. Orientation measurement performance for pumping modulation compared to engineered PSFs. (a) VUB Γ_{jj} of modulating pumping polarization for measuring the in-plane second moments m_1, m_2, and m_4. (b) Sum R_Σ of the diagonal entries of the CRB matrix $\mathbf{R}$ over the m_1, m_2, and m_4 moments averaged over the entire 3D orientation space versus the sum Γ_Σ of the diagonal elements of the VUB matrix $\mathbf{\Gamma}$ over the m_1, m_2, and m_4 moments. Blue: polarized PSF, red: defocused PSF, yellow: bisected PSF, purple: tri-spot PSF, green: pumping polarization modulation. Dark line: $R_\Sigma = \Gamma_\Sigma$.

of each in-plane second moment m_j (Figure 4(a)) and find that pumping modulation has a relatively uniform precision across the three second moments. We next compare pumping modulation to other engineered PSFs, calculating the full 3D $\mathbf{\Gamma}$ using Equation (9) but using the sum Γ_Σ for the 1st, 2nd and 4th second moments to compare measurement performance. Note that restricting the pumping polarization to be within the xy plane causes the measurement to be sensitive to only the in-plane second moments $\langle \mu_x^2 \rangle$, $\langle \mu_y^2 \rangle$, and $\langle \mu_x \mu_y \rangle$, even for

molecules tilted out of the xy plane. Perhaps unsurprisingly, pumping modulation shows the best estimation precision for the in-plane orientational second moments (Figure 4(b)). Again, we found that VUB-predicted measurement performance is consistent with that given by the average CRB.

4. CONCLUSION

We demonstrate a variance upper bound (VUB) for fast quantification and comparison of orientation measurement techniques. Calculating the VUB is ~1000 times faster than computing the average CRB with sufficient sampling over orientation space at a cost of reducing accuracy by ~34%. VUB-based comparisons of different orientation measurement techniques are consistent with those given by the average CRB. Given its computational efficiency, VUB has great potential for optimizing schemes for SM orientation measurement in real-time.

ACKNOWLEDGMENTS

REFERENCES

[1] Backer, A. S., Biebricher, A. S., King, G. A., Wuite, G. J., Heller, I., and Peterman, E. J., "Single-molecule polarization microscopy of DNA intercalators sheds light on the structure of S-DNA," *Science Advances* **5**(3) (2019).

[2] Wang, M., Marr, J. M., Davanco, M., Gilman, J. W., and Liddle, J. A., "Nanoscale deformation in polymers revealed by single-molecule super-resolution localization-orientation microscopy," *Materials Horizons* **6**(4), 817–825 (2019).

[3] Novotny , L. and Hecht, B., [*Principles of Nano-Optics*], Cambridge University Press (2006).

[4] Böhmer, M. and Enderlein, J., "Orientation imaging of single molecules by wide-field epifluorescence microscopy," *JOSA B* **20**(3), 554–559 (2003).

[5] Backer, A. S., Backlund, M. P., von Diezmann, A. R., Sahl, S. J., and Moerner, W., "A bisected pupil for studying single-molecule orientational dynamics and its application to three-dimensional super-resolution microscopy," *Applied physics letters* **104**(19), 193701 (2014).

[6] Zhang, O., Lu, J., Ding, T., and Lew, M. D., "Imaging the three-dimensional orientation and rotational mobility of fluorescent emitters using the tri-spot point spread function," *Applied physics letters* **113**(3), 031103 (2018).

[7] Backer, A. S., Lee, M. Y., and Moerner, W., "Enhanced dna imaging using super-resolution microscopy and simultaneous single-molecule orientation measurements," *Optica* **3**(6), 659–666 (2016).

[8] Rao, C. R., Rao, C. R., Statistiker, M., Rao, C. R., and Rao, C. R., [*Linear statistical inference and its applications*], vol. 2, Wiley New York (1973).

[9] Kay, S. M., [*Fundamentals of statistical signal processing*], Prentice Hall PTR (1993).

[10] Lieb, M. A., Zavislan, J. M., and Novotny, L., "Single-molecule orientations determined by direct emission pattern imaging," *JOSA B* **21**(6), 1210–1215 (2004).

[11] Backer, A. S. and Moerner, W., "Extending single-molecule microscopy using optical fourier processing," *The Journal of Physical Chemistry B* **118**(28), 8313–8329 (2014).

[12] Backer , A. S. and Moerner, W., "Determining the rotational mobility of a single molecule from a single image: a numerical study," *Optics express* **23**(4), 4255–4276 (2015).